Optics Communications 489 (2021) 126875

Contents lists available at ScienceDirect

Optics Communications

journal homepage: www.elsevier.com/locate/optcom

Energy flux optimization in 1D multiperiodic four-component photonic crystals

Ivan S. Panyaev [a], Dmitry G. Sannikov [a,*], Nataliya N. Dadoenkova [a,b], Yuliya S. Dadoenkova [c,a]

[a] Ulyanovsk State University, 432017 Ulyanovsk, Russian Federation
[b] Donetsk Institute for Physics and Engineering named after A. A. Galkin, Donetsk 83114, Ukraine
[c] Lab-STICC (UMR 6285), CNRS, ENIB, 29238 Brest Cedex 3, France

ARTICLE INFO

Keywords:
Photonic crystal
Energy fluxes
Photonic bandgap

ABSTRACT

The results of theoretical and numerical studies of finite one-dimensional (1D) three-periodic photonic crystals of the structure $[(ab)^3(cd)^3]^3$, consisting of four different materials (dielectric oxides Al_2O_3, SiO_2, TiO_2, and ZrO_2) are presented. We study the transmittivity spectra and partial energy fluxes of the TE- and TM-modes in the range of 1–5 μm in the vicinity of the first photonic bandgap depending on the incidence angle and frequency of light. The obtained results can be used to create precise polarization-sensitive devices for an input–output of the radiation into an optical fiber. The optimization of the considered multiperiodic structures has been achieved at the telecommunication wavelength 1.55 μm both by changing incidence angle and adjusting the topology (i.e. thicknesses of the constituent layers). We discuss a principle of a new type of polarization splitter on the basis of three-periodic photonic crystal.

1. Introduction

The control of light in photonic crystals (PC), *i.e.*, materials with periodic modulation of the refractive index, strongly depends on the band structure. The propagation of light is forbidden inside the photonic bandgaps (PBGs) [1–4]. The PBGs exist due to multiple interference of the electromagnetic waves reflected and refracted at each boundary between the layers of the PC. As a rule, when designing a PC, it is preferable to have its PBG with clearly defined frequencies of the center and the edges.

In addition to the conventional 1D PCs in the form of periodic layered structures based on two materials (for example, *a* and *b*), "ternary" PCs consisting of three materials *a*, *b*, and *c* with different refractive indices, *i.e.*, $(abc)^M$ structures, have been recently proposed [5–7]. The dispersion relation for these structures was obtained in several papers (see, for example, [8,9] and references therein). The PBG modification with changing the layer thicknesses and the refractive indices in a ternary PC with a left-handed medium has been studied in Ref. [10], including the cases of oblique incidence of TE- and TM-polarized light.

Multicomponent PC structures can be successfully used in telecommunication devices, such as tunable multichannel filters (see, for example, [11] and references therein), narrow-channel transmission-type filters for wavelength division multiplexing systems [12], etc. In a recent work [13], the conditions and controllability of interface states are investigated in 1D photonic structures composed of two binary layered PC, having the same photonic bandgaps but different unit cells, which can be used for the fabrication of the effective multichannel narrowband filters. Also we note paper [14], where a reconfigurable optical bandpass filter with flat-top transmission line and narrow band in nanometer scale is designed using two coupling prisms and a sandwiched planar optical waveguide. In [15], spectral polarization-independent filter designs with a large angle of incidence, based on 1D PCs containing a negative-index defect layer, have been proposed. 1D PCs with alternating layers of negative permittivity materials and negative permeability metamaterials can be used for design of tunable filters at the microwave frequency range [16].Ternary PCs containing, for example, a polymer [17] or a superconductor [18], can serve as temperature sensors. A study of the simultaneous determination of gas concentration and temperature in 1D PC was performed in [19]. The presence of the defect modes in the spectra of such PCs can be also used in various branches of medicine. For instance, in [20], a method for detecting cancer cells by registering the shift of the transmission peaks in the spectra of a 1D nanocomposite material with a PC coating has been proposed. When considering biosensors based on 1D PC, an improvement in volumetric and surface sensitivity is observed [21]. In the recent article [22], a new quasi-periodic structure on the base of a 1D plasma photonic crystal where an omnidirectional bandgap is obtained along with the polarization splitting effect is proposed. We should also note a recent paper [23], in which the heterostructure formed by two different PCs with a metallic layer inclusion is proposed to produce a split topological state.

* Correspondence to: Ulyanovsk State University, 432017, 42 L.Tolstoy str., Ulyanovsk, Russian Federation.
E-mail address: sannikov-dg@yandex.ru (D.G. Sannikov).

https://doi.org/10.1016/j.optcom.2021.126875
Received 2 October 2020; Received in revised form 5 February 2021; Accepted 13 February 2021
Available online 18 February 2021

1D PCs have been successfully used with fluorescent amplifying devices [24] and color displays [25]. In addition, 1D multicomponent crystals [26] can be used in thermophotoelectric devices. The random dielectric multilayers following a white-noise-like pattern can be used as solar concentrators and random lasers [27]. It was theoretically predicted that a PC filter deposited on the surface of a diode should provide strong bonding of all electromagnetic radiation modes at the frequencies above the PBG and should not provide coupling of low-frequency modes [28]. The 1D PC consisting of the stack of cholesteric liquid crystal and the equidistant isotropic medium layers have shown at certain conditions some potential advantages (e.g. multicolored reflection) over a single layer [29]. In Ref. [30], it is shown that systems based on 1D PCs of the type $(HL)^M HDH(LH)^M$ (H and L are high- and low-refractive layers and D is a defect) containing a four-level atomic medium, allow nonlinear all-optical switching at ultra-low intensities of the coupling and switching laser fields.

To ensure the rearrangement of the transmission spectra of the ternary PC $(abc)^M$, one can create a new type of a regular 1D structure with two periods, where the internal finite-size block $(ab)^N$ is inside a unit cell $[(ab)^N c]$ repeated M times. For the first time, these systems were considered as photonic–magnonic crystals [31–35] and were studied as photonic hypercrystals [36–39]. In Ref. [7], the spectral peculiarities of the bi-periodic structure $[(TiO_2/SiO_2)^N\ Al_2O_3]^M$ are demonstrated, and the differences between the PBG spectra of the ternary $(TiO_2/SiO_2/Al_2O_3)^N$ dielectric PCs are shown. Ternary structures based on bi-periodic planar magnetic PCs can also be implemented in the lower frequency region [40].

In [41], a wide class of composite three-periodic photonic crystals of the structure $[(ab)^N(cd)^M]^K$ has been considered, and their classification has been proposed based on the optical contrast of the pairs of layers forming the construction blocks, *i.e.*, the absolute value and sign of the difference in the permittivities of the materials. The intraband (defect) modes in the transmission spectra, their number and resonant frequencies, which can be adjusted by changing the parameters of the PC structure and the incidence angle of the electromagnetic waves, have been studied. This paper contains the development of our work [41] and discussion concerning possible practical applications of the obtained results. Here we investigate a three-periodic four-component 1D PC structure $[(ab)^N(cd)^M]^K$ with the same number of sub- and supercells ($M = N = K = 3$). We show that its transmission spectra have wide well-pronounced PBGs with clear boundaries, which, in particular, determines its potential practical value. We study the partial energy fluxes of the modes in the vicinity of the first PBG depending on the incidence angle and the frequency of light, as well as the "transverse" intensity emitted from the side surface of the PC. Based on the results of the analysis, we discuss the possibility of creation of precise polarization-sensitive radiation input–output devices for the use in integrated and fiber optics.

The paper is organized as follows. Section 2 presents the geometry of the three-periodic PC and general analysis. In Section 3, we show results of the numerical calculations of the transmittivity spectra, partial energy flux in the subcells and transverse energy fluxes. In Section 4, we discuss a principle of a polarization-splitting device based on multiperiodic PC. Section 5 summarizes the obtained results.

2. Description of the system

Let us consider a multiperiodic 1D PC of a finite size created on the base of four different dielectric layers a, b, c, and d with the thicknesses l_a, l_b, l_c, and l_d, respectively. A PC supercell can be formed by combining two periodic subcells which consist of different pairs of materials (for example, blocks ab and cd) repeated N and M times, respectively. The thicknesses of the blocks (ab) and (cd) are $L_1 = l_a + l_b$ and $L_2 = l_c + l_d$, and the thickness of the supercell is $L_3 = NL_1 + ML_2$. By translating the supercell K times, one obtains the structure $[(ab)^N(cd)^M]^K$, as shown schematically in Fig. 1. Thus, this system is a 1D three-periodic PC, consisting of "internal" subcells $(ab)^N$ and $(cd)^M$, forming a supercell $(ab)^N(cd)^M$. The total thickness of the structure is KL_3 (Fig. 1).

The electromagnetic plane wave of the wavelength λ in vacuum (the angular frequency ω) is incident on the left-hand side of the structure under an incidence angle θ, so that the (xz) is the plane of incidence. The optical system is isotropic, and the TE- and TM-modes are the eigenstates of the electromagnetic wave.

To calculate the electromagnetic fields in the three-periodic PC, the transfer matrix method is used, described in detail in Ref. [41].

The transverse non-zero Umov–Poynting vector components (with respect to the PC growth axis, which in the chosen geometry coincides with the z-axis) are related to the electric **E** and magnetic **H** fields as follows:

$$S_x^{\mathrm{TE}}(z) = \frac{c}{8\pi}\mathrm{Re}(E_y H_z^*), \quad S_x^{\mathrm{TM}}(z) = -\frac{c}{8\pi}\mathrm{Re}(E_z H_y^*) \tag{1}$$

for TE- and TM-modes, respectively, with c being the speed of light in vacuum. Note that $S_x(z)$ can be considered as a "transverse" intensity, which can be output from the side surface of the PC (along the x-axis).

The longitudinal components of the fluxes (with respect to the PC growth axis), expressed as

$$S_z^{TE}(z) = -\frac{c}{8\pi}\mathrm{Re}(E_y H_x^*), \quad S_z^{TM}(z) = -\frac{c}{8\pi}\mathrm{Re}(E_x H_y^*) \tag{2}$$

are constant [7].

The partial energy fluxes of the electromagnetic wave in the structure are found as follows. We integrate the transverse components of the energy density within the corresponding limits of each individual layer of the type j and sum them by the number X of the type-j layers:

$$P_j = \sum_X \int_{z_{\mathrm{left}}}^{z_{\mathrm{right}}} S_x(z)\,dz, \tag{3}$$

where z_{left} and z_{right} are left- and right-hand boundaries of the type-j layer. Thus, e.g., the partial linear flux P_c [erg/(μm s)] is the sum of the fluxes in all the layers of the type c.

3. Numerical results and discussion

For the layers a, b, c, and d we choose the dielectric oxides TiO_2, SiO_2, Al_2O_3, and ZrO_2. These materials are transparent in visible and near infra-red regimes. The frequency dispersion of their refractive indices is described by the Sellmeier equations [42–45] in the wavelength range (1–5) μm and is shown in Fig. 2. The difference between the refractive indices of the materials can be interpreted as the optical contrast. Here we denote the optical contrast of the pair of layers as *high* ("***h***") if the difference between the refractive indices of the materials is larger than 1, whereas if the difference is less than 0.5, the optical contrast is *low* "***l***". This is shown in Fig. 2 by vertical dashed lines. The intermediate state with the medium optical contrast between 0.5 and 1 is described in details in Ref. [41], and it is out of the consideration in this paper.

In this section, we show results of the numerical calculation of the transmittivity spectra and energy fluxes in the three-periodic four-component PC, where the left-hand-side subcell is formed by materials with high optical contrast (TiO_2 and SiO_2), and the right-hand-side subcell is formed by materials with low optical contrast (Al_2O_3 and ZrO_2). For simplicity, we use the following notations of the oxides: T for TiO_2, Z for ZrO_2, A for Al_2O_3, and S for SiO_2. According to the classification of four-component three-periodic PCs based on the absolute values and signs of the permittivity contrast between the pairs of layers forming the unit cell introduced in our paper [41], such multiperiodic structure belongs to the ***hl*** group (subgroup $\boldsymbol{h^+l^-}$, the superscripts "+" and "–" refer to the sign of the optical contrast) and is characterized by well-pronounced PBGs with vertical edges and several narrow intraband modes. The optimal number of the sub- and supercells ensuring well-pronounced PBG edges is $M = N = K = 3$. Thus, here and after we consider the three-periodic structure $[(TS)^3(AZ)^3]^3$.

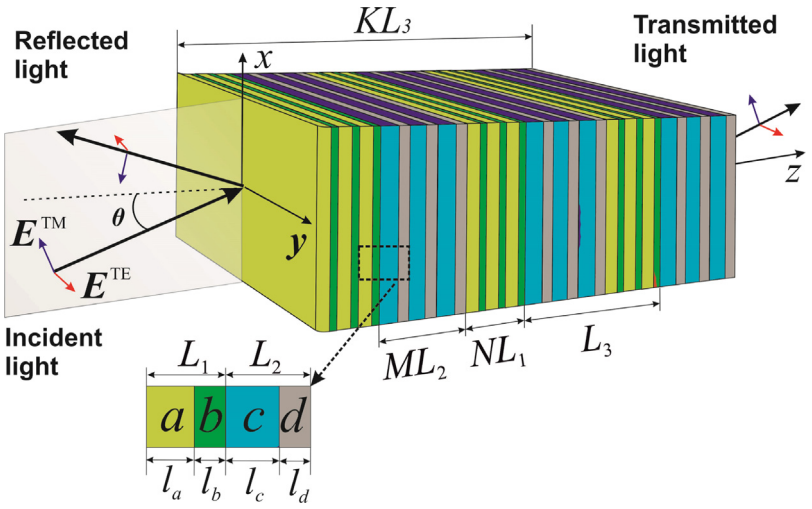

Fig. 1. Schematic of 1D dielectric three-periodic four-component PC of the structure $[(ab)^N(cd)^M]^K$ for $N = M = K = 3$. Here $\mathbf{E}^{TE}$ and $\mathbf{E}^{TM}$ denote the electric fields of TE- and TM-polarized light, and θ is the incidence angle.

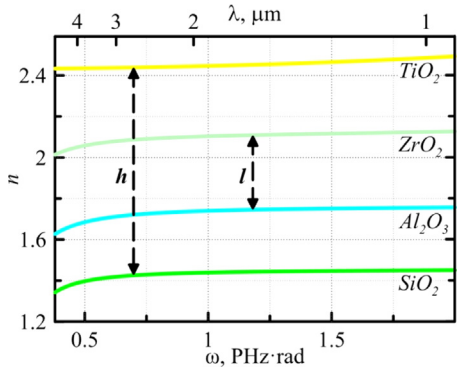

Fig. 2. Refractive indices of the PC constituents (TiO_2, SiO_2, Al_2O_3, and ZrO_2) *versus* the angular frequency ω (or the wavelength λ).

We chose the layer thicknesses l_j in order to satisfy the Bragg resonance condition in each layer at the wavelength λ_h for the high-optical-contrast pairs of layers T and S and λ_l for low-optical-contrast layers A and Z [41]:

$$n_{T,S}(\lambda_h)\, l_{T,S} = \frac{\lambda_h}{4}, n_{A,Z}(\lambda_l)\, l_{A,Z} = \frac{\lambda_l}{4}, \tag{4}$$

where n_j is the refractive index of the layer j. Note that λ_h and λ_l in our case are different and correspond to the PBG centers of the PCs formed by the high- and low-optical-contrast cells (TS) and (AZ), respectively.

3.1. Transmittivity spectra and partial fluxes in multiperiodic photonic crystal

We start our analysis with calculation of the transmittivity spectra of TE- and TM-modes for the simple PC structures $(TS)^{NK}$ and $(AZ)^{MK}$ constituting the three-periodic structure $[(TS)^N(AZ)^M]^K$ with $M = N = K = 3$. The PBG centers are at $\lambda_h = 1.5$ μm and $\lambda_l = 2$ μm (which corresponds to the angular frequencies $\omega_h = 1.257$ rad PHz and $\omega_l = 0.942$ rad PHz, respectively). The thicknesses of the layers in this case are shown in the first line in Table 1 using Eq. (4).

Fig. 3 shows the transmission spectra of TE- and TM-polarized light in the structures $(TS)^{18}$ (left-hand-side column), $(AZ)^{18}$ (central column) and $[(TS)^3(AZ)^3]^3$ (right-hand-side column). As can be seen from Figs. 3(a), 3(d) and 3(b), 3(e), the PBG of the structure $(TS)^{18}$ is much wider, sharper and has more pronounced boundaries in comparison to the PBG of the structure $(AZ)^{18}$. This is due to the higher optical contrast of the constituents of the (TS) cell. The spectral properties of single-periodic PC $(TS)^{18}$ with high optical contrast dominate in the formation of the PBG of the multiperiodic structure (Figs. 3(c) and 3(f)). Indeed, its opaque region remains near the frequency ω_h of the PBG center of the structure $(TS)^{18}$. Despite the fact that none of the PC subcells have any defect layer, the resulting PBG of three-periodic PC contains series of intraband transmission modes which can be treated as defect modes formed by the low-optical-contrast subcells $(AZ)^3$ acting as complex defect layers separating the $(TS)^3$ subcell.

Fabrication of various micro- and nanostructures of new generation via the radiation of the predefined distribution from a side surface of the PC (so-called "light patterning", for instance, for photolithographic purposes [46]), requires detailed analysis of the intensity flux. We provide the analysis of the partial fluxes on the side surface of the multiperiodic structures.

Fig. 4 shows the ratios of partial energy fluxes P_{TS}/P_{AZ} between the subcells $(TS)^3$ and $(AZ)^3$ constituting the structure, where $P_{TS} = P_T + P_S$ and $P_{AZ} = P_A + P_Z$, with P_j ($j = T, S, A, Z$) being the linear flux in the jth layer (in erg/(μm· s), see Eq. (3)). For the structure $[(TS)^3(AZ)^3]^3$ with $\lambda_h = 1.5$ μm, $\lambda_l = 2$ μm (the upper panel), the flux in the spectral regions corresponding to the transmission intraband modes is higher in the subcell $(AZ)^3$ with low optical contrast (the blue bands $P_{TS}/P_{AZ} < 1$), whereas in the PBG regions, the high optical contrast subcell $(TS)^3$ gives a larger contribution to the flux (*i.e.*, the red and the yellow bands, where the ratio $P_{TS}/P_{AZ} > 1$). With an increase of the incidence angle, the value P_{TS}/P_{AZ} in the PBG strongly increases ($P_{TS}/P_{AZ} >> 1$) for the case of TE-polarization state, as one see from Fig. 4(a). The opposite dependence is observed for TM-polarization [see Fig. 4(b)], which is associated with a simultaneous broadening of the PBG for TE-polarized state and a narrowing of the PBG for TM-polarized electromagnetic waves. With the rearrangement of the wavelengths of the centers of the PBGs ($\lambda_h \leftrightarrow \lambda_l$) of the high- and low-optical-contrast subcells [$\lambda_h = 2$ μm, $\lambda_l = 1.5$ μm], the energy contribution of the (TS) subcells in the PBG regions is retained and even more pronounced for TE- and TM-modes [Figs. 4(c) and 4(d)], however, in the regions of the transmission bands the predominance of the energy flux in the (AZ) subcells becomes noticeably smaller. This happens due to the change in the optical contrast of the layers forming the subcells, and, consequently, due to the change of the thicknesses of the corresponding layers. Indeed, changing λ_h and λ_l lead to change of the dielectric permittivities of the materials due to dispersion, which, in turn, leads to different thicknesses of the layers satisfying the Bragg condition Eq. (4) – see numerical values in the first and the second lines in Table 1.

Table 1
Wavelengths λ_h and λ_l and angular frequencies ω_h and ω_l of the PBG centers of the high- and low-optical-contrast subcells $(TS)^N$ and $(AZ)^M$ of the three-periodic structure and the corresponding thicknesses of the layers l_T, l_S, l_A, and l_Z.

λ_h (μm)	λ_l (μm)	ω_h (rad PHz)	ω_l (rad PHz)	l_T (μm)	l_S (μm)	l_A (μm)	l_Z (μm)	KL_3 $[(TS)^3(AZ)^3]^3$ (μm)	KL_3 $(TS)^{18}$ (μm)	KL_3 $(AZ)^{18}$ (μm)
1.5	2.0	1.257	0.942	0.153	0.260	0.288	0.238	8.451	7.434	9.468
2.0	1.5	0.942	1.257	0.205	0.348	0.215	0.178	8.514	9.954	7.074
1.8	1.72	1.047	1.096	0.184	0.312	0.247	0.204	8.523	8.928	8.118

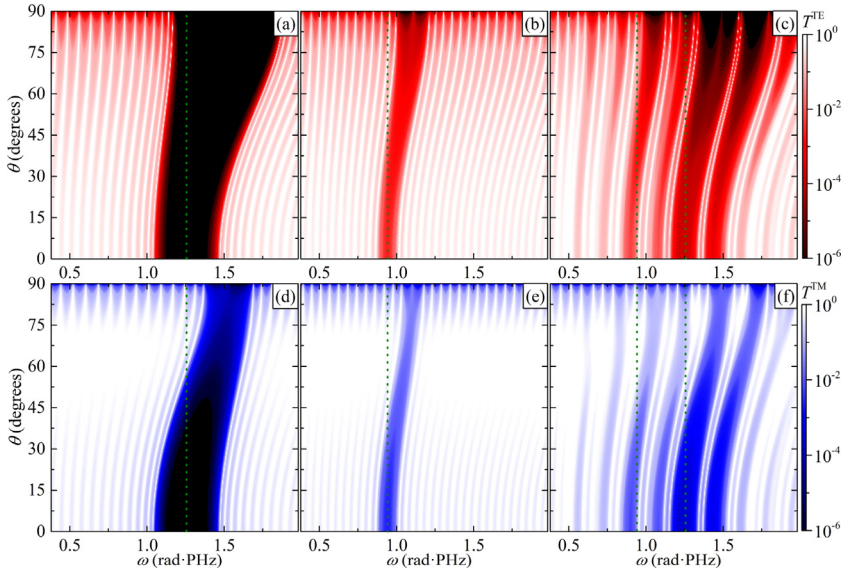

Fig. 3. Transmittivity of TE- (the upper panel) and TM-modes (the bottom panel) depending on the angular frequency ω and the incidence angle θ of light for the different structures: (a, d) $(TS)^{18}$, λ_h = 1.5 μm (ω_h = 1.257 rad PHz); (b, e) $(AZ)^{18}$, λ_l = 2 μm (ω_{0l} = 0.942 rad PHz); (c, f) $[(TS)^3(AZ)^3]^3$, for λ_h = 1.5 μm, λ_l = 2 μm. The frequencies of the PBG centers are marked with vertical green dotted lines.

Note that the choice of the position and width of the PBG of the subcell by the variation of λ_h and λ_l and the numbers of the periods N and M (*i.e.*, modification of the transmission spectra of the subcells $(TS)^N$ and $(AZ)^M$ constituting the three-periodic PC) allows to design the preferable form of the "resulting" PBG of the whole multiperiodic structure [41].

The position of the centers of the PBGs of the high-optical-contrast and low-optical-contrast subcells and (λ_h and λ_l) makes it possible to change the resulting transmission spectrum, the energy fluxes in the composite PC structure, as well as the light intensity S_x inside the structure, as can be seen from the discussion below.

3.2. Transverse energy fluxes in multiperiodic photonic crystal

In this section, we analyze the transverse energy flux in the three-periodic PC whose high- and low-optical-contrast subsystems have PBG centers at the wavelengths λ_h = 1.8 μm (angular frequency ω_h = 1.047 rad PHz) and λ_l = 1.72 μm (ω_l = 1.096 rad PHz), and the thicknesses of the layers are shown in the bottom line of Table 1. These values are chosen in order to obtain closely located but distinguishable intraband TE- and TM-modes in the resulting transmission spectrum for the specific operating wavelength λ_0 = 1.55 μm.

The distribution of the transverse component of the energy flux density $S_x(\theta, z)$ is illustrated in Fig. 5(a) as function of the incidence angle θ and the coordinate z inside the PC for the input radiation of the wavelength λ_0 = 1.55 μm (corresponding to the angular frequency ω = 1.215 rad PHz), the red and the blue color corresponds to TE- and TM-modes, respectively. In Figs. 5 and 6 the values of the intensity S_x are in erg/(μm$^2\cdot$ s). Here we consider the incidence angles corresponding to the transmission peaks for TE- and TM-polarized light. The vertical cyan (up-pointing triangles) and violet (down-pointing triangles) lines correspond to the cross-section profiles $S_x(\theta)$ at the fixed coordinates z = 1.4 μm and z = 4.0 μm, respectively, for TE- and TM-polarizations, shown in Fig. 5(b). The horizontal green (circles) and blue (squares) lines correspond to the cross-section profiles $S_x(z)$ for the fixed incidence angle θ = 28.7° and θ = 27.6° for TE- and TM-modes, respectively, illustrated in Fig. 5(c). The gray vertical lines in Figs. 5(a) and 5(c) indicate the boundaries of the layers of the structure: solid, dash-dotted, dashed, and dotted lines indicate the coordinates of the left-hand-side interfaces of the layers T, S, A, and Z, respectively.

Fig. 5(d) shows the transmission spectra of the structure $[(TS)^3(AZ)^3]^3$ as functions of the incidence angle θ at the fixed wavelength of the incoming light λ_0 = 1.55 μm (ω = 1.215 rad PHz) for TE- (cyan line) and TM- polarized light (violet line). These spectra contain two pronounced transmittance peaks for both TE- and TM-polarized light. The spectrum of the TE-modes is characterized by narrower transmission peaks at θ = 28.7° and θ = 38°, whereas the PBG of the TM-modes is characterized by wider intraband transmission peaks at θ = 27.6° and θ = 40°. With an increase of the incidence angle, one can observe an increase of the transmittivity of the TM-polarized light and the transmittivity decrease of the TE-polarized electromagnetic wave due to the narrowing of the defect modes of TE-modes and the broadening of those of TM-modes.

The peaks of the energy flux density in the structure depending on the incidence angle $S_x(\theta)$ [Fig. 5(b)] at the fixed value of the z-coordinate are observed at the same incidence angles as the peaks of the transmission spectrum [Fig. 5(d)]. Mathematically, this is explained by the fact that both quantities (T and S_x) are quadratic functions of the amplitude of the electric (for TE-modes) and magnetic (for TM-modes) fields. Indeed, the transmission coefficient can be written in general form as the ratio of the squared moduli of the amplitudes of the transmitted and incident waves:

$$T^{TE} = \left|\frac{E_t}{E_i}\right|^2, \quad T^{TM} = \left|\frac{H_t}{H_i}\right|^2 \tag{5}$$

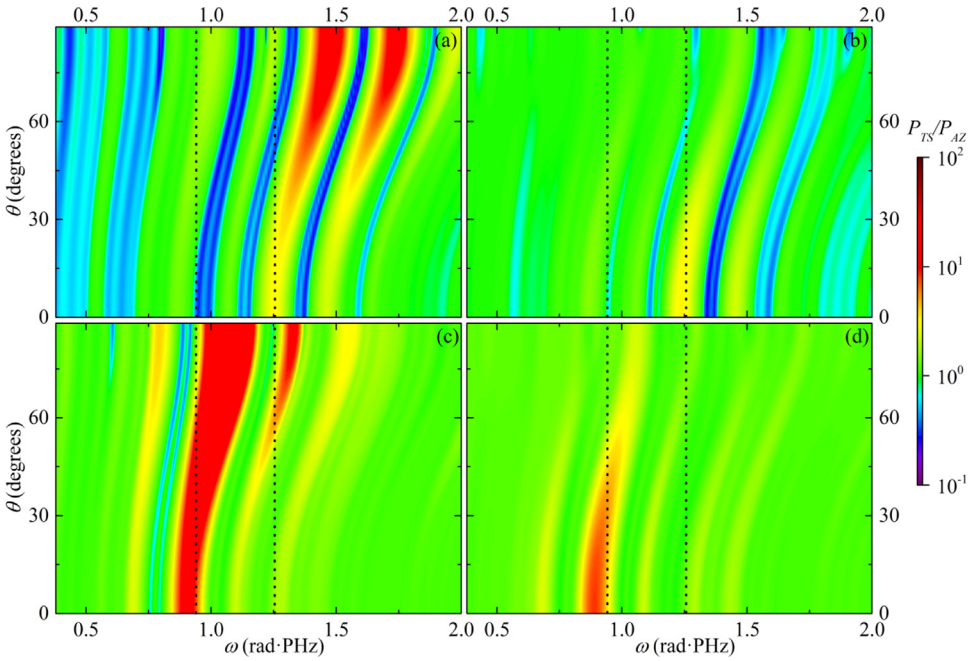

Fig. 4. Partial energy fluxes between the subcells *TS* and *AZ* of the structure $[(TS)^3(AZ)^3]^3$ with λ_h = 1.5 μm (ω_h = 1.257 rad PHz), λ_l = 2 μm (ω_l = 0.942 rad PHz) (the upper panel) and λ_h = 2 μm, λ_l = 1.5 μm (the bottom panel). The frequencies of the PBG centers are marked with vertical dotted black lines. The left-hand-side and right-hand-side columns show TE- and TM-modes, respectively.

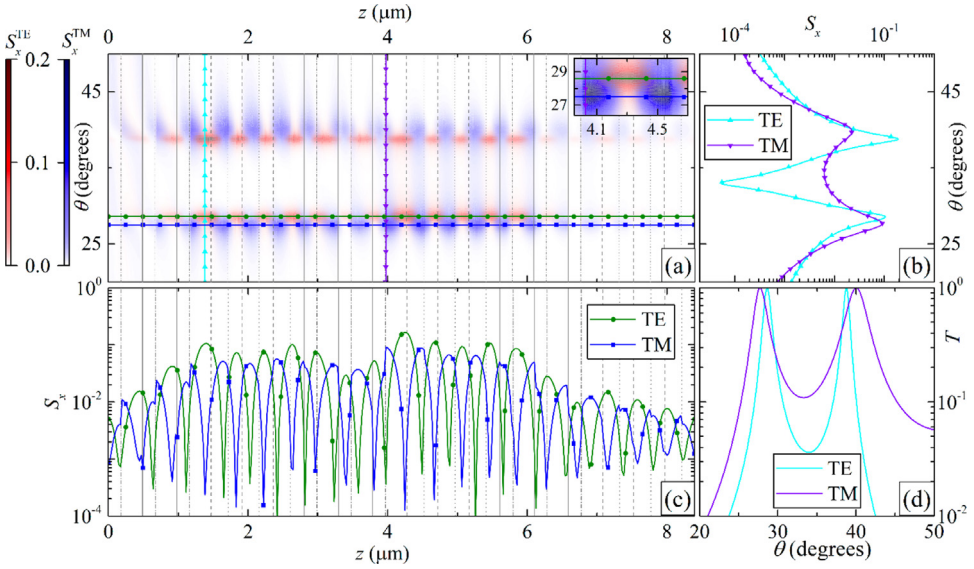

Fig. 5. (a) The transverse component of the energy flux density $S_x(\theta, z)$ for TE- (red palette) and TM- (blue palette) modes. The inset zooms the region 26.5°< θ < 29.5° and 4 μm < z < 4.7 μm. (b) Angular dependencies $S_x(\theta)$ at z = 1.4 μm for TE-mode (cyan vertical line in (a), up-pointing triangles) and z = 4.025 μm for TM-mode (violet vertical line in (a), down-pointing triangles). (c) Distribution profiles $S_x(z)$ at θ = 28.7° for TE-mode (green horizontal line in (a), circles) and θ = 27.6° for TM-mode (blue horizontal line in (a), squares). (d) Transmission spectra $T(\theta)$. The PC structure is $[(TS)^3(AZ)^3]^3$ with the PBG centers of the subcells $(TS)^3$ and $(AZ)^3$ at the wavelengths λ_h = 1.8 μm (ω_h = 1.047 rad PHz) and λ_l = 1.72 μm (ω_l = 1.096 rad PHz). The operating wavelength is λ_0 = 1.55 μm (ω = 1.215 rad PHz).

On the other hand, in Eq. (1) for the energy flux S_x, the amplitudes of the electric and magnetic fields can be expressed through each other using the Maxwell's equations.

The TE-polarized modes are in average several times higher in intensity and possess more pronounced dip between the $S_x(\theta)$ peaks than in the case of the TM-polarized light. A characteristic feature of the distribution of $S_x(z)$, as can be seen from Figs. 5(a) and 5(c), is an alternation of the peaks and dips of the TE- and TM-polarized modes, or the so-called "checkerboard" arrangement: the maxima of S_x of the TE-modes correspond to the minima of S_x for the TM-modes for the adjacent defect modes. For this reason, the profiles $S_x(\theta)$ for the TE- and TM-polarized light are given in Fig. 5(c) for different values of the longitudinal coordinate z = 1.4 μm and z = 4.0 μm, respectively.

Now we will analyze the spectral dependence of the transverse flux. The distribution of the transverse component of the energy flux density $S_x(\omega, z)$ is shown in Fig. 6(a) as function of the angular frequency ω and the coordinate z inside the PC for the fixed value of the incidence angle θ = 28°. As can be seen from Fig. 6(a) and its inset, outside the PBG (for ω < 0.9 rad PHz and ω > 1.4 rad PHz), the alternation of the peaks and dips of S_x of the TE- and TM-polarized light (the "checkerboard" arrangement) is well preserved for the neighboring transmission bands. The inset in Fig. 6(a) shows the distribution of the intensities of the TE-

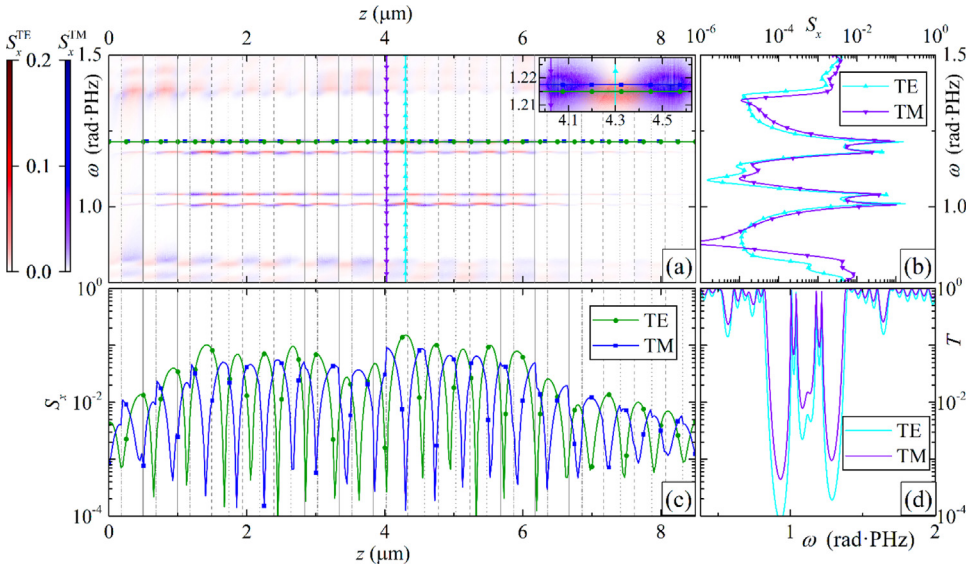

Fig. 6. (a) The transverse component of the energy flux density $S_x(\omega, z)$ for TE- (red palette) and TM- (blue palette) modes. The inset zooms the region $4 < z < 4.6$ μm and $1.21 < \omega < 1.225$ rad PHz. (b) Frequency dependencies $S_x(\omega)$ at $z = 4.0$ μm for TE-mode (cyan vertical line in (a), up-pointing triangles) and $z = 4.3$ μm for TM-mode (violet vertical line in (a), down-pointing triangles). (c) Distribution profiles $S_x(z)$ at $\omega = 1.215$ rad PHz for TE-mode (green horizontal line in (a), circles) and $\omega = 1.217$ rad PHz for TM-mode (blue horizontal line in (a), squares). (d) Transmission spectra $T(\omega)$. The structure is $[(TS)^3(AZ)^3]^3$ with the PBG centers at the wavelengths $\lambda_h = 1.8$ μm ($\omega_h = 1.047$ rad PHz) and $\lambda_l = 1.72$ μm ($\omega_l = 1.096$ rad PHz). The angle of incidence is $\theta = 28°$.

and TM-intraband modes within the PC region $4 < z < 4.6$ μm around the frequency $\omega = 1.215$ rad PHz ($\lambda = 1.55$ μm). The distribution profiles $S_x(\omega)$ at the fixed coordinate $z = 4.0$ μm (Fig. 6(b)) for TE-mode (cyan line, up-pointing triangles) and $z = 4.3$ μm for TM-mode (violet line, down-pointing triangles) are similar to the corresponding transmission spectra $T(\omega)$ in the PBG region: two pairs of S_x peaks are at the same frequencies as the corresponding transmittivity peaks. Moreover, for the TE-mode, the amplitudes of S_x are higher than those for the TM-polarized light. However, outside the PBG, the values of $S_x(\omega)$ for both TE- and TM-polarizations are, in average, one order of magnitude lower than the peak values of the intraband modes, despite the fact that the value of T in these regions reaches 1. This can take place due to the bandwidth effect, *i.e.*, the narrower the band is, the higher the energy flux density S_x becomes.

The transmission spectra $T(\omega)$ for the fixed incidence angle $\theta = 28°$ for the TE- and TM-polarization states are shown in Fig. 6(d). Each of the spectra contains two pairs of narrow close defect modes within the PBG at the frequencies around $\omega \sim 1.06$ rad PHz ($\lambda \sim 1.74$ μm) and $\omega \sim 1.215$ rad PHz ($\lambda \sim 1.55$ μm). The PBG itself has very sharp boundaries (note the logarithmic scale of the ordinate axis) at the frequencies 0.9 rad PHz and 1.4 rad PHz.

Thus, the narrow transmission peaks inside the PBG (defect modes) make the largest contribution to the distributions of the transverse component of the energy flux density $S_x(\omega, z)$ and $S_x(\theta, z)$, which should be taken into account when designing multiperiodic PC structures for integrated optics devices.

4. Practical use

Optimization of multiperiodic PC allows us to obtain a predefined intensity distribution at the side surface of the structure. This light patterning, which can be interpreted as an analogue of a mask in the typical exposure optical system in lithography [46], is flexible due to the discussed above polarization sensitivity of the multiperiodic PC. For example, one can interchange or overlap the maxima and minima of the light intensity of the different polarizations on the lateral surface by rotating the polarization plane of the input light. The positions of the maxima and minima themselves are specified by the boundaries of the layers. This tunable polarization sensitivity (the switching of the field intensity distribution) can be an advantage of such a mask

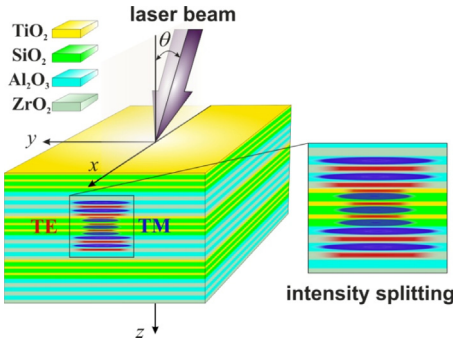

Fig. 7. Schematic of multiperiodic PC structure operating as a polarization splitter. The spatial splitting of the energy fluxes of TE- and TM-modes on the side surface of the PC (along z-axis) is shown by the red and the blue color distributions.

in comparison with a conventional one used in lithography. Note that composite photonic structures can be realized easily by standard electron beam evaporation technology, opening more possible applications in multichannel narrowband filters and other optical modulation devices [13].

Specific spatial distribution of the flux of TE- and TM-modes in multiperiodic PC shown in Fig. 5 can be used in a principle of a polarization-splitting device. Indeed, a laser beam bounded in the transverse direction at an incidence angle with a certain spread (for example, at $\theta = 28°$ with $\Delta\theta \approx 1.5°$) will produce peaks in the energy flux density of the electromagnetic wave on the side surface of the structure at different positions for the TE- and TM-polarizations (in the case illustrated in Fig. 5, at $z = 1.4$ μm (TE-mode) and $z = 4.0$ μm (TM-mode)), *i.e.*, the peaks will be spatially separated. This can be applied in polarization sensors and splitters on the basis of such PC structures at the wavelength 1.55 μm. In Fig. 7 we show the schematic of a such a polarization splitter.

5. Conclusions

We have analyzed the incidence angle dependence, spectral, and energy characteristics of the TE- and TM-modes transmitted through

multiperiodic photonic crystal structure $[(ab)^N(cd)^M]^K$ with the same number of sub- and superperiods $M = N = K = 3$. The spectra of such photonic crystal in the near-IR regime (in the range of 1-5 μm) have pronounced and wide photonic bandgaps with vertical boundaries. The positions of the edges and of the center of the bandgap are defined by the spectral properties of the high-optical-contrast subcell, whereas the presence of the intraband (defect) modes is determined by the properties of the low-optical-contrast subcell.

We have shown that the peaks and dips of the transverse component of the energy flux density of the TE- and TM-modes alternate at the intraband modes, *i.e.* have the "checkerboard" arrangement. For TM-polarized light, the transverse energy flux dependences strongly "blur" with the increase of the incidence angle, which is associated with a broadening of the transmission mode. For the TE-mode, the opposite effect is observed: transmission modes are broader at smaller angles, and the fluxes are more diffuse with a decrease of the incidence angle. In addition, we have demonstrated that by changing the incidence angle, it is possible to create highly efficient optical filters with a tunable pair of wavelengths. The behavior of such a distribution of power fluxes is similar to the transmission spectrum of the structure.

It is shown that the transmission spectra of three-periodic photonic crystals can be designed by adjustment of the corresponding wavelengths of the centers of the bandgaps of the multiperiodic PC subcells (and, as a consequence, the thicknesses of the layers). The considered structures can be easy to implement, since they do not require the use of special defect impurities (semiconductors, superconductors, polymers, etc.). For example, one can configure the transmission spectrum of the structure in such a way that there is a group of intraband transmission modes for each polarization state of light at the fixed wavelength or in its vicinity. On the basis of this structure, it is possible to fabricate a polarization-sensitive angle sensor with a given accuracy. Apart from that, the polarization sensitivity allows to apply this structure as a light pattern mask in modern lithography.

Also, due to specificity of the transverse energy flux distribution on the side surface of the photonic crystal, polarization-sensitive devices for the precision input–output of the radiation into an optical fiber can be proposed. The adjustable accuracy of the shift of the transmission mode in the angle or frequency is important when working with broadband laser sources (for example, semiconductor ones).

CRediT authorship contribution statement

Ivan S. Panyaev: Investigation, Software, Visualization, Conceptualization, Writing - original draft . **Dmitry G. Sannikov:** Conceptualization, Data curation, Supervision, Writing - original draft. **Nataliya N. Dadoenkova:** Supervision, Conceptualization, Methodology, Writing - review & editing. **Yuliya S. Dadoenkova:** Conceptualization, Data curation, Writing - review & editing.

Declaration of competing interest

The authors declare that they have no known competing financial interests or personal relationships that could have appeared to influence the work reported in this paper.

Acknowledgments

The reported study was funded by RFBR, Russia, project number 19-42-730008 (I.S.P., D.G.S., N.N.D., and Y.S.D.). Y.S.D. acknowledges support from École Nationale d'Ingénieurs de Brest under the project CF-SPEACS, Conseil Régional de Bretagne, France, under the project SPEACS, and Programme PAUSE of the Collège de France, the Ministry of Higher Education and Science of the Russian Federation (Project "Development of comb-spectrum generators for applications in microwave photonics, spectroscopy, and high-speed data processing").

References

[1] J.D. Joannopoulos, S.G. Johnson, J.N.J. Winn, R.D. Meade, Photonic Crystals. Molding the Flow of Light, second ed., Prinstone University Press, Princeton, 2008.
[2] R.B. Wehrspohn, H.-S. Kitzerow, K. Busch (Eds.), Nanophotonic Materials, Wiley-VCH, Berlin, 2008, http://dx.doi.org/10.1002/9783527621880.
[3] K. Sakoda, Optical Properties of Photonic Crystals, second ed., Springer, Berlin, 2005, http://dx.doi.org/10.1017/CBO9781107415324.004.
[4] Q. Gong, X. Hu, Photonic Crystals: Principles and Applications, Pan Stanford, 2014.
[5] X.F. Xu, J.Y. Ding, A wide band-pass filter of broad angle incidence based on one-dimensional metallo-dielectric ternary photonic crystal, Opt. Quantum Electron. 41 (2009) 1027–1032, http://dx.doi.org/10.1007/s11082-010-9415-x.
[6] N.H. Rafat, S.A. El-Naggar, S.I. Mostafa, Modeling of a wide band pass optical filter based on 1D ternary dielectric-metallic-dielectric photonic crystals, J. Opt. 13 (2011) 085101, http://dx.doi.org/10.1088/2040-8978/13/8/085101, (8pp).
[7] N.N. Dadoenkova, Y.S. Dadoenkova, I.S. Panyaev, D.G. Sannikov, I.L. Lyubchanskii, One-dimensional dielectric bi-periodic photonic structures based on ternary photonic crystals, J. Appl. Phys. 123 (2018) http://dx.doi.org/10.1063/1.5011637, 043101–043108.
[8] S.K. Awasthi, R. Panda, L. Shiveshwari, Multichannel tunable filter properties of 1D magnetized ternary plasma photonic crystal in the presence of evanescent wave, Phys. Plasmas. 24 (2017) 072111–072117, http://dx.doi.org/10.1063/1.4989703.
[9] S. Wang, X. Yang, C.T. Liu, Omnidirectional reflection in one-dimensional ternary photonic crystals and photonic heterostructures, Phys. Lett. A. 378 (2014) 1326–1332, http://dx.doi.org/10.1016/j.physleta.2014.03.010.
[10] Z. Zare, A. Gharaati, Investigation of band gap width in ternary 1D photonic crystal with left-handed layer, Acta Phys. Pol. A. 125 (2014) 36–38, http://dx.doi.org/10.12693/APhysPolA.125.36.
[11] S. Roshan Entezar, Photonic crystal wedge as a tunable multichannel filter, Superlattices Microstruct. 82 (2015) 33–39, http://dx.doi.org/10.1016/j.spmi.2015.01.039.
[12] M. Zamani, Photonic crystal-based optical filters for operating in second and third optical fiber windows, Superlattices Microstruct. 92 (2016) 157–165, http://dx.doi.org/10.1016/j.spmi.2016.02.025.
[13] D. Gao, W. Mao, R. Zhang, J. Liu, Q. Zhao, W.Y. Tam, X. Wang, Tunable interface state in one dimensional composite photonic structure, Opt. Commun. 453 (2019) 124324, http://dx.doi.org/10.1016/j.optcom.2019.124324.
[14] J. Liu, L. Tao, Reconfigurable flat-top narrow bandpass filter in prism pair coupled planar optical waveguide, Opt. Commun. 459 (2020) 125038, http://dx.doi.org/10.1016/j.optcom.2019.125038.
[15] K.Y. Xu, X. Zheng, C.L. Li, W.L. She, Design of omnidirectional and multiple channeled filters using one-dimensional photonic crystals containing a defect layer with a negative refractive index, Phys. Rev. E - Stat. Nonlinear, Soft Matter Phys. 71 (2005) http://dx.doi.org/10.1103/PhysRevE.71.066604.
[16] Y. Zhang, W.-H. Zhu, G.-H. Ding, Tunneling modes induced by interface states in 1D photonic crystals with single negative materials, J. Appl. Phys. 127 (2020) 213104, http://dx.doi.org/10.1063/5.0001618.
[17] D.M. El-Amassi, S.A. Taya, D. Vigneswaran, Temperature sensor utilizing a ternary photonic crystal with a polymer layer sandwiched between Si and SiO2 layers, J. Theor. Appl. Phys. 12 (2018) 293–298, http://dx.doi.org/10.1007/s40094-018-0308-x.
[18] J. Wu, J. Gao, Analysis of temperature-dependent optical properties in 1D ternary superconducting photonic crystal with mirror symmetry, J. Supercond. Nov. Magn. 28 (2015) 1971–1976, http://dx.doi.org/10.1007/s10948-015-3002-0.
[19] Y.H. Chen, W.H. Shi, L. Feng, X.Y. Xu, M.Y. Shang-Guan, Study on simultaneous sensing of gas concentration and temperature in one-dimensional photonic crystal, Superlattices Microstruct. 131 (2019) 53–58, http://dx.doi.org/10.1016/j.spmi.2019.05.033.
[20] N.R. Ramanujam, I.S. Amiri, S.A. Taya, S. Olyaee, R. Udaiyakumar, A. Pasumpon Pandian, K.S. Joseph Wilson, P. Mahalakshmi, P.P. Yupapin, Enhanced sensitivity of cancer cell using one dimensional nano composite material coated photonic crystal, Microsyst. Technol. 25 (2019) 189–196, http://dx.doi.org/10.1007/s00542-018-3947-6.
[21] S.M. Lo, S. Hu, G. Gaur, Y. Kostoulas, S.M. Weiss, P.M. Fauchet, Photonic crystal microring resonator for label-free biosensing, Opt. Express 25 (2017) 7046, http://dx.doi.org/10.1364/oe.25.007046.
[22] Y. Ma, H. Zhang, C.X. Hu, Tunable omnidirectional band gap and polarization splitting in one-dimensional magnetized plasma photonic crystals with a quasi-periodic topological structure, J. Opt. (United Kingdom) 22 (2020) http://dx.doi.org/10.1088/2040-8986/ab613d.
[23] N.J. Bianchi, L.M. Kahn, Optical states in a 1D superlattice with multiple photonic crystal interfaces, J. Opt. (United Kingdom) 22 (2020) http://dx.doi.org/10.1088/2040-8986/ab896c.
[24] K. Min, S. Choi, Y. Choi, H. Jeon, Enhanced fluorescence from CdSe/ZnS quantum dot nanophosphors embedded in a one-dimensional photonic crystal backbone structure, Nanoscale 6 (2014) 14531–14537, http://dx.doi.org/10.1039/c4nr03907f.

[25] H. Shen, Z. Wang, Y. Wu, B. Yang, One-dimensional photonic crystals: fabrication, responsiveness and emerging applications in 3D construction, RSC Adv. 6 (2016) 4505–4520, http://dx.doi.org/10.1039/C5RA21373H.
[26] V.A. Tolmachev, T.S. Perova, K. Berwick, Design of one-dimensional composite photonic crystals with an extended photonic band gap, J. Appl. Phys. 99 (2006) 033507, http://dx.doi.org/10.1063/1.2165401, (5pp).
[27] J. Escorcia-García, M.E. Mora-Ramos, Optical reflectivity and spatial mode localization of white-noise random dielectric oxide multilayers, Opt. Commun. 432 (2019) 1–7, http://dx.doi.org/10.1016/j.optcom.2018.09.043.
[28] I. Celanovic, F. O'Sullivan, M. Ilak, J. Kassakian, D. Perreault, Design and optimization of one-dimensional photonic crystals for thermophotovoltaic applications, Opt. Lett. 29 (2004) 863–865, http://dx.doi.org/10.1364/OL.29.000863.
[29] A.H. Gevorgyan, Resonant interaction of light with a stack of alternating layers of a cholesteric liquid crystal and an isotropic medium, Phys. Rev. E - Stat. Nonlinear, Soft Matter Phys. 92 (2015) 062501, http://dx.doi.org/10.1103/PhysRevE.92.062501.
[30] V.G. Arkhipkin, S.A. Myslivets, All-optical switching in a photonic crystal with a defect containing an N-type four-level atomic system, Phys. Rev. A - At. Mol. Opt. Phys. 86 (2012) 063816, http://dx.doi.org/10.1103/PhysRevA.86.063816.
[31] J.W. Kłos, M. Krawczyk, Y.S. Dadoenkova, N.N. Dadoenkova, I.L. Lyubchanskii, Photonic-magnonic crystals: Multifunctional periodic structures for magnonic and photonic applications, J. Appl. Phys. (2014) http://dx.doi.org/10.1063/1.4874797.
[32] Y.S. Dadoenkova, N.N. Dadoenkova, I.L. Lyubchanskii, J.W. Klos, M. Krawczyk, Confined states in photonic-magnonic crystals with complex unit cell, J. Appl. Phys. 120 (2016) http://dx.doi.org/10.1063/1.4961326, 073903–073909.
[33] J.W. Klos, M. Krawczyk, Y.S. Dadoenkova, N.N. Dadoenkova, I.L. Lyubchanskii, Spin waves and electromagnetic waves in photonic-magnonic crystals, IEEE Trans. Magn. 50 (2014) 2–5, http://dx.doi.org/10.1109/TMAG.2014.2321532.
[34] Y.S. Dadoenkova, N.N. Dadoenkova, J.W. Kłos, M. Krawczyk, I.L. Lyubchanskii, Goos-Hänchen effect in light transmission through biperiodic photonic-magnonic crystals, Phys. Rev. A. 96 (2017) 043804–043806, http://dx.doi.org/10.1103/PhysRevA.96.043804.
[35] Y.S. Dadoenkova, N.N. Dadoenkova, I.L. Lyubchanskii, J.W. Klos, M. Krawczyk, Faraday effect in bi-periodic photonic-magnonic crystals, IEEE Trans. Magn. 53 (2017) 1–5, http://dx.doi.org/10.1109/TMAG.2017.2712278.
[36] E.E. Narimanov, Photonic hypercrystals, Phys. Rev. X. 4 (2014) 1–13, http://dx.doi.org/10.1103/PhysRevX.4.041014.
[37] V.N. Smolyaninova, B. Yost, D. Lahneman, E.E. Narimanov, I.I. Smolyaninov, Self-assembled tunable photonic hyper-crystals, Sci. Rep. 4 (2015) 5706, http://dx.doi.org/10.1038/srep05706, (9 pp).
[38] S.V. Zhukovsky, A.A. Orlov, V.E. Babicheva, A.V. Lavrinenko, J.E. Sipe, Photonic-band-gap engineering for volume plasmon polaritons in multiscale multilayer hyperbolic metamaterials, Phys. Rev. A - At. Mol. Opt. Phys. 90 (2014) 013801, http://dx.doi.org/10.1103/PhysRevA.90.013801, (11 pp).
[39] A.V. Chebykin, V.E. Babicheva, I.V. Iorsh, A.A. Orlov, P.A. Belov, S.V. Zhukovsky, Enhancement of the purcell factor in multiperiodic hyperboliclike metamaterials, Phys. Rev. A. 93 (2016) 033855, http://dx.doi.org/10.1103/PhysRevA.93.033855, (9 pp).
[40] A. Girich, A. Kharchenko, S. Tarapov, Spectral features of a multi-periodical metamaterials, in: Proc. Int. Conf. Adv. Optoelectron. Lasers, CAOL, IEEE, 2019, pp. 408–411, http://dx.doi.org/10.1109/CAOL46282.2019.9019522.
[41] I.S. Panyaev, L.R. Yafarova, D.G. Sannikov, N.N. Dadoenkova, Y.S. Dadoenkova, I.L. Lyubchanskii, One-dimensional multiperiodic photonic structures: A new route in photonics (four-component media), J. Appl. Phys. 126 (2019) 103102, http://dx.doi.org/10.1063/1.5115829, (11 pp).
[42] I.H. Malitson, Interspecimen comparison of the refractive index of fused silica, J. Opt. Soc. Amer. 55 (1965) 1205–1209, http://dx.doi.org/10.1364/JOSA.55.001205.
[43] J.R. Devore, Refractive indices of rutile and sphalerite, J. Opt. Soc. Amer. 41 (1951) 416–419, http://dx.doi.org/10.1364/JOSA.41.000416.
[44] D.L. Wood, K. Nassau, Refractive index of cubic zirconia stabilized with yttria, Appl. Opt. 21 (1982) 2978–2981, http://dx.doi.org/10.1364/AO.21.002978.
[45] I.H. Malitson, M.J. Dodge, Refractive index and birefringence of synthetic sapphire, J. Opt. Soc. Amer. 62 (1972) 1405, http://dx.doi.org/10.1364/JOSA.62.001336.
[46] T. Ito, S. Okazaki, Pushing the limits of lithography, Nature 406 (2000) 1027–1031, http://dx.doi.org/10.1038/35023233.